JP1.13 A COMPARISON OF TWO MELLOR-YAMADA-BASED PBL SCHEMES IN SIMULATING A HYBRID BARRIER JET

Joseph B. Olson * and John M. Brown

NOAA Earth System Research Laboratory, Boulder, CO, US

1. INTRODUCTION

The coastal meteorology of southeastern Alaska frequently consists of intense orographically enhanced winds. Inland cold pools develop as air cools over the interior and accelerates downs the terrain, resulting in strong winds manifested as gap and channel flows, and downslope windstorms depending in the location and synoptic situation. The latter are locally known as "Taku" windstorms (Dierking 1998; Colman and Dierking 1992; Bond et al. 2006). High wind events can extend from the inland waterways to the coast when a low pressure system over the Gulf of Alaska is combined with a high pressure system over northwestern Canada, producing an ambient pressure gradient conducive for accelerating the inland cold pools through the coastal mountain gaps (Colle et al. 2006). Furthermore, coastal gap outflows can then merge with ambient coastal barrier jets to form hybrid barrier jets (Loescher et al. 2006; Winstead et al. 2006). Strong turbulent mixing can occur at the confluent interface between the gap outflow and the ambient onshore flow (Olson et al. 2008).

To our knowledge, there have been no detailed studies of the TKE within statically stable gap flows or hybrid barrier jets. The turbulent mixing within these jets will likely regulate their strength, structure, and duration. Accurate modeling of stable boundary layers within mesoscale models has been quite challenging, since commonly observed intermittent turbulence (Nappo 1991; Mahrt 1999, 1998; Howell and Sun 1997; Blumen et al. 2001) violates the assumption of steady-state theory. The ability of current and next-generation operational weather forecast models to simulate the formation of an inland cold pool, their subsequent contribution to coastal gap outflows, and their interaction with coastal barrier jets needs to be assessed.

The Advanced Research version of the Weather Forecasting Model (WRF-ARW) (Skamarock et al. 2008) has become host to several planetary boundary layer (PBL) schemes in the past few years. The testing and validation of these and older PBL schemes in the WRF-ARW is important because of the increased emphasis on the prediction of near-surface variables such as wind, ceiling and visibility, as well as the increasing use of WRF-ARW for operational forcasting. A TKE-based schemed called the Mellor-Yamada-Nakanishi-Niino (MYNN) (Nakanishi and Niino 2004) has recently been integrated into the WRF-ARW. This scheme has potential to help reduce some of the common biases associated with the Mellor-Yamada-Janjić (MYJ) (Janjić 2002) scheme, such as shallow PBL height and low temperature bias (Zhang and Zheng 2004). Model biases of both schemes are relatively unknown in regions of complex terrain and need to be identified and diagnosed in order to further system development.

The case study chosen for analysis was taken from the Southeastern Alaskan Regional Jets (SARJET) experiment, which investigated the structures and physical processes of barrier jets along the coastal mountains near Juneau, Alaska (Winstead et al. 2006). This study investigates the performance of the WRF-ARW over the complex coastal orography of Alaska, with focus on the spatial and temporal structure of the hybrid barrier jet and TKE produced by two different TKE-based PBL scemes. The intent is to uncover the reasons why each scheme produces a different structural evolution. To do so, each component of the eddy diffusivity coefficient, K_ϕ,

$$K_\phi = q l_m S_\phi, \tag{1}$$

where $q = TKE^{1/2}$, l_m is the mixing length scale, S_ϕ is a dimensionles stability function, and ϕ can represent momentum, heat, or moisture, will be analyzed within the hybrid barrier jet. High-resolution model simulations are compared with measurements sampled by the Wyoming King-air research aircraft and ground-based profilers to assess the accuracy of each PBL scheme.

2. EXPERIMENTAL SETUP

a. Model configuration

The WRF-ARW version 3.1 [see Skamarock et al. (2008) for a description of v3.0; changes for v3.1 relevant to this study are minor] was configured for three domains: 13, 4.33, and 1.44 km, using one-way nesting (Fig. 1). Each domain consists of 51 full σ-levels in the vertical, with eight model levels below $\sigma = 0.9$ and ∼14 levels below 700 mb. The coarse domain is large enough to capture the landfalling cyclones, but does not sufficiently resolve steep coastal mountains and sea-level gaps with width $\leq$O(50 km). However, the coarse domain provides a benchmark for testing the expected advantage of the high-resolution nests, which better resolve the complex coastal orography and mountain-induced circulations.

The initial and boundary conditions were provided by NCEP Global Forecast System (GFS) analyses at 0.5-deg resolution every 6 hours. The sea-surface temperatures were obtained from the daily NCEP SST analysis. All model configurations used the RUC land-surface model (Smirnova et al. 2000). The Grell-Devenyi cumulus parameterization (Grell and Devenyi 2002) on the 13-km domain, while the grid scale precipitation processes for all domains were represented by the Thompson six-class microphysical scheme (Thompson et al. 2004). The Rapid Radiative Transfer Model (RRTM) (Mlawer et al. 1997) was used to parameterize radiative processes. This model also employs a gravity wave absorption layer in order to prevent gravity waves from being reflected off the model top.

The boundary layer turbulent mixing was parameterized with two separate schemes. The first TKE-based scheme implemented into the WRF-ARW was the MYJ PBL scheme (Janjić 2002), which is a 2.5 level closure model. A recent addition to the WRF-ARW, the MYNN PBL scheme (Nakanishi and Niino 2004) is also a level 2.5 closure TKE-based scheme but can be configured to run at 3.0 level closure as well. For a direct comparison, we utilize the 2.5 level configuration herein. Both schemes utilize the same form of the TKE equation, but differ in their formulations of mixing length scales, l_m, and were tuned to different data sets: the MYJ was tuned to observations while the MYNN was tuned to large-eddy simulations (LES). The potential advantage of LES is that they provide a whole range of turbulence statistics throughout the entire PBL under controllable conditions. The idealized conditions exclude irregularities caused by nonstationary, transitional, or mesoscale phenomena, which may contaminate observed data (Esau and Byrkjedal 2007). A detailed description of the differences between these two PBL schemes is found in Appendix A.

b. *Data processing*

Flight-level measurements were obtained from the University of Wyomings King-Air research aircraft. These measurements consist of in situ observations from south of Cross Sound (pt. A in Fig. 1c) to near Yakutat (pt. D), and from southwest-northeast flight legs at various altitudes between the coast (pt. C) and 120 km offshore (pt. E). This flight pattern was completed twice (in two separate flights) during this IOP and will be referred to as flight 1 and flight 2, respectively.

Flight data sampled at 10-Hz was used to compute the TKE $[(u'^2 + v'^2 + w^2)/2]$. Here u' and v' are the along-wind and cross-wind perturbations, respectively. The mean wind components were obtained from 30 s averages along the flight legs transecting the barrier jet. This averaging period yields independent estimates separated by roughly 3 km in the horizontal direction and an average of 150 m in the vertical direction. The deviations were then computed as the difference between the intantaneous measurements and the mean.

3. SYNOPTIC AND MESOSCALE OVERVIEW

At 1200 UTC 12 October 2004 (Fig. 1a), there was a broad surface low over the Aleutian Islands with ridging over western Canada and southerly flow over the Gulf of Alaska. A secondary surface cyclone was forming over the baroclinic region over the Gulf of Alaska (Fig. 1a). At 1800 UTC (Fig. 1b), the secondary low ($\sim$998 mb) moved northeastward towards the southeastern coast of Alaska with an associated weak trough positioned $\sim$500 km offshore. The corresponding model solution using the MYJ PBL (Fig. 1) accurately captures the depth and placement of the large-scale features.

By 0000 UTC 13 October 2004 (Fig. 1c), the trough came within 300 km of the coast and the associated low pressure system intensified to near 995 mb. The offshore-directed pressure gradient force in the coastal region has intensified as the landfalling trough moved closer to the inland ridge. This acts to accelerate the inland cold pool through the Cross Sound, producing a cold gap outflow of $\sim$20 m s^{-1}. The combination of onshore flow with the gap outflow results in a strong coastal hybrid jet with wind speeds near 30 m s^{-1} (shown later). A more detailed description of this event can be found in Olson et al. (2008).

4. STRUCTURE AND EVOLUTION OF THE TKE WITHIN THE HYYBRID JET

The observed winds and derived TKE are shown in the vertical cross-sections between pts C-E for both flights (Fig. 2). The cold gap outflow over slightly warmer sea-surface temperatures (SST) resulted in weak surface heat fluxes, which produced buoyancy-generated TKE within the hybrid jet beneath 250 m ASL (Fig. 2a). This combined with shear-generated TKE in the surface layer to produce TKE of 0.5-2.0 m^2 s^{-2} in the lowest flight leg (150 m MSL). During the second flight (Fig. 2b), a strong shear-layer developed between the offshore-directed gap outflow ($\sim$400 m MSL) and the onshor (southerly) flow aloft ($\sim$1000 m MSL). This resulted in a reduction of the local Richardson number to $\sim$0.25. The observed maximum TKE increased to 2-6 m^2 s^{-2} and became elevated at the outer edge of the gap outflow (400-500 m MSL) with another maximum above the gap outflow (near 1000 m MSL).

Model cross-sections of 1.44 km domain terrain-parallel wind speed, TKE, and potential temperature between pts. C-E for both the MYJ and MYNN are shown in Fig. 3.

Prior to the begining of flight 2, at 2300 UTC (Figs. 3a,b), the coast-parallel wind speeds are dominated by gap outflow, with a wide wind speed maxima located near $\sim$600 ($\sim$800) m MSL in the MYJ (MYNN) simulation. The simulated TKE max is located at the surface with values < 1 m^2 s^{-2} (> 2 m^2 s^{-2}) in the MYJ (MYNN). At 0100 UTC (Figs. 3c,d), which is most representative of the flight 2 observations (Fig. 2), both simulations intensify the hybrid barrier jet (to $\sim$25 m s^{-1}) and developed strong vertical shear, resulting in an elevated TKE values of $\sim$1 m^2 s^{-2} (> 3 m^2 s^{-2}) in the MYJ (MYNN). Although the depth of the jet is better simulated in the MYJ, the width and magnitude of TKE is better simulated in the MYNN. Note the much stronger vertical wind shear in lowest 200 m in the MYJ simulation, which has surface coast-parallel wind speed of $\sim$14 m s^{-1} beneath the jet max compared to $\sim$19 m s^{-1} in the MYNN.

At 0300 UTC (Figs. 3d,e), the hybrid jet narrowed as the trough moved over the gap outflow, further increasing the vertical wind shear. The slightly faster advancing trough in the MYNN simulation acts to weaken the hybrid jet faster than in the MYJ simulation. Since the MYJ PBL scheme was "less active" in mixing out the strong shear layer, the resolveable dynamics are left to reduce the dynamic instability. This results in the generation of Kelvin-Helmholtz (K-H) instability over the gap outflow. Since the model can only barely resolve this feature ($\sim$6 $\triangle$x wavelength) and the column-mixing of the 1-D PBL scheme effectively mixes out the K-H billows, the result is a strong gravity wave feature.

The spatial extent of the model hybrid barrier jet and TKE structures are shown in (Fig. 4). Both PBL schemes produced the largest values of TKE in the region of the gap outflow, upstream of the C-E cross-sections. This was due to stronger vertical wind shear as well as stronger surface heat fluxes (not shown). As the trough moved into the region of the gap outflow (Figs. 4e,f), the coastal jet narrowed and the outer edge of the maximum TKE became sharper. The maximum simulated TKE at 500 m MSL remained >5 m^2 s^{-2} in this region in the MYNN simulation. Both PBL schemes produce a TKE field that appears advected in nature, but there is no TKE advection in standard release of WRF-ARW. The effects of TKE advection will be explored in the following section to see if this impacts the magnitude of the TKE reaching the C-E fligh legs.

5. PBL SCHEME BEHAVIOR WITHIN THE HYBRID JET

a. *Analysis of the diffusivity coefficients*

The three components comprising the diffusivity coefficients (Eq. 1): the TKE, mixing length scale, and stability functions are analyzed in a vertical profile extending through the hybrid barrier jet at a point located in the middle of the hybrid barrier jet ($\sim$50 km southwest of the coast). Figure 5 shows each component along with the product, the eddy diffusivity K_m (bottom Figs. 5g,h), for both the MYJ (left) and MYNN (right). As noted in the previous subsection, the TKE in much larger in the MYNN than in the MYJ simulation. A period of enhanced turbulent mixing between 0100 and 0200 UTC results in a maximum of $\sim$1.5 m^2 s^{-2} ($\sim$3 m^2 s^{-2}) in the MYJ (MYNN) simulation (Figs. 5a,b).

The mixing length scales, l_m, for each PBL scheme also differ by a 30-50%, with the maximums in the boundary layer of $\sim$60 m (80-90 m) in the MYJ (MYNN) simulation (Figs. 5c,d). Since the MYJ mixing length is heavily dependent on the amount of TKE (Eq. A4), it is no surprise that the mixing length is much smaller than in the MYNN, which also has a turbulent length scale of similar form to (Eq. A4), but has an addition buoyancy length scale (Eq. A8) which can dominate in stable conditions. Also, the formulation of the mixing length in the MYNN scheme is not dependent on whether it is within or outside the PBL as in the MYJ PBL scheme. Therefore, larger mixing length scales extend beyond the depth of the hybrid jet in the MYNN, but are capped beneath the top of the jet in the MYJ. This limits the mixing between the ambient onshore flow and the gap outflow in the MYJ simulation.

The stability functions, S_m, differ even more so between the two PBL schemes (Figs. 5e,f). The MYJ has a dual maximum (0.4-0.6) in the surface layer and above the PBL, while the MYNN has a maximum of similar magnitude in the surface layer as well as a thin maximum at the top of the hybrid jet and at the base of the landfalling trough, which descends as the trough moves over the jet region (01-04 UTC). The stability function acts as a constraint, which modulates the product of the three components, K_m, such that the model mixing is realistic for a given mean atmospheric profile. This may explain why a scheme with low TKE and l_m may still yield a reasonable K_m and therefore, reasonable overall turbulent mixing.

The eddy diffusivity for momentum, K_m, for each scheme is shown in figures 5g,h. Both schemes have maximum in thte bottom of the PBL and are halved by the middle of their respective PBLs. The maximums are 20-25 m^2 s^{-1} ($\sim$40 m^2 s^{-1}) in the MYJ (MYNN) PBL scheme. The same quantities for heat behave similar to their momentum counterparts (not shown), except for the stability functions for heat, S_h, which are shallower for both PBL schemes and do not have a secondary maximum above the gap outflow in the MYNN PBL.

The turbulent Prandtl number ($\mathrm{Pr} = K_m/K_h$) for each scheme is shown as a function of the Richardson Number,

$$Ri = \left(\frac{g}{\Theta_0}\right)\frac{\partial\Theta_v/\partial z}{\left(\partial U/\partial z\right)^2 + \left(\partial V/\partial z\right)^2}, \qquad (2)$$

throughout the same profile analyzed in Figure 5 for hours 22-03 UTC 12-13 October 2004 (Fig. 6). In the MYJ scheme, the Pr $\geq$1 for all Ri, with a maximum of $\sim$1.15 for 0.2 < Ri < 1.1. In contrast, the Pr for the MYNN behaves more similarly to that found in other observational and LES studies, with Pr < 1 for Ri < 0.2, but increasing to 2-5 for Ri of 2-5. Although these results are only valid within the hybrid jet, the fairly large range of Ri sampled suggests that the MYNN PBL may better parameterize the relative mixing of heat and momentum throughout a variety of atmospheric conditions.

b. PBL tendencies

The tendencies computed from each PBL scheme are shown in figure 7. The tendencies are computed as the partial derivative of product of the eddy diffusivities and the mean vertical gradients,

$$\frac{\partial \phi}{\partial t} = \frac{\partial}{\partial z}\left(K_{\phi}\frac{\partial \phi}{\partial z}\right), \tag{3}$$

so variation of the background mean variables has been added to figure 7. Despite the much larger eddy diffusivities found in the MYNN PBL scheme, the overall magnitude of the momentum tendencies are similar between the two schemes. This is because, as noted in the vertical cross-section across the hybrid jet (Fig. 3), the low-level vertical wind shear was much greater in the MYJ. This compensates for the smaller K_m found in the MYJ scheme. The deceleration of the low-level winds is mostly confined to under 500 m MSL in both schemes, but the MYNN scheme is much less variable with time. Also, the turbulent mixing episode at 01-02 UTC results in the acceleration of the coast-parallel wind above 1000 m MSL in the MYNN, while only reaching 800 m MSL in the MYJ simulation.

The temperature tendencies (Fig. 7c,d) are slightly larger in the MYNN than in the MYJ, since the ambient stratification is more comparable between the two simulations, so the vertical potential temperature gradient can not compensate for the smaller K_h in the MYJ PBL scheme. The temperature tendencies are largest for both schemes when the gap outflow is strongest (21-23 UTC) and acts to transfer heat to the gap outflow from the warmer sea-surface, while cooling the warmer onshore flow that mixes with the upper portion of the gap outflow. The temperature tendencies fluctuate in strength in both simulations, but are discontinuous in the MYJ and are confined to a more shallow extent (< 800 m MSL) compared to the MYNN (> 1500 m MSL).

The moisture tendencies are of the same magnitude in each scheme (Fig. 7e,f), with values of +0.2-0.5 g kg^{-1} hr^{-1} within the hybrid jet region. Like the other tendencies, they are more vertically distributed in the MYNN and more steady in time than in the MYJ simulation.

6. EFFECTS OF TKE ADVECTION

The role of TKE advection was investigated to see if the TKE structures within the hybrid barrier jet could be better simulated and whether this would impact the evolution of the kinematic and thermal structure of the barrier jet. Although the dissipation rate of TKE can be relatively large compared to advection for coarse grid simulations (> 10 km), the advection of TKE can be significant on smaller scales where larger gradients can exist. The WRF-ARW was altered to advect TKE using the monotonic advection of Wang et al. (2009) and an addidtional "TKEADV" experiment was conducted using the MYNN PBL scheme. The following analysis focuses on the 1.44 km domain during the time period when the hybrid barrier jet was at or near maximum intensity (0200 UTC 13 October 2004).

The top two panels of figure 8 show a comparison of the TKE in a vertical cross-section along C-E (Fig. 1c) through the hybrid barrier jet. The main difference is that the maximum TKE become smaller and slightly less spread in the vertical. This creates a slightly smoother field, without the tower of TKE along the coast in the original simulation (Fig. 8). The impact on the wind speed and stratification within the hybrid barrier jet is negligible (<1 m s^{-1} difference in the wind speed maximum). This results is consistent with other hours examined (not shown). The same effect can be see in the 500 m winds and TKE for the control simulation (Fig. 8c) and TKEADV (Fig. 8d). The TKE becomes not only smoother field in the vicinity of the coastal jet, but the many small scale ($\sim$5 $\triangle x$) maxima near Cross Sound become smoothed out.

The slight overall decrease in TKE is likely due to the feedback between the model mixing length predicted by the MYNN PBL scheme, which is dependent upon the TKE (see apppendix A). If TKE is initially decreased by smoothing a maxima, the PBL scheme will produce a smaller l_m. A smaller l_m will result in a larger dissipation term in the TKE equation (Eq. A1). This could lead to smaller values to TKE to be advected into neighboring gridpoints (non-source regions), leading to an overall reduction of TKE. It is unclear whether the smoother field obtained by advection helps to increase the numerical stability of the WRF-ARW since, but it is concievable that a more well behaved field may improve numerical stability in other situations.

7. SUMMARY AND CONCLUSIONS

The hybrid barrier jet case presented here shows the mean and turbulent structure of a low-level jet with maximum speeds exceeding $\sim$25 m s^{-1} produced by a landfalling cyclone off the southeastern coast of Alaska. Early in the event, the largest values of TKE were located near the surface, where cold gap outflow over warmer SSTs resulted in buoyancy produced TKE. Later in the event, as the landfalling cyclone neared the coastal region, the ambient winds became oriented more southerly (onshore). This acted to increase the wind shear above the gap outflow, resulting in enhanced shear-generated TKE near in the upper portion of the hybrid barrier jet.

The barrier jet was well simulated my both PBL schemes. The MYNN (MYJ) PBL simulated the best temperature, wind direction and TKE (wind speed) verified against aircraft observations. However, the vertical structure of the hybrid barrier jet was better simulated by the MYJ, since the stronger shear layer resulted in K-H waves, which better match flight observations.

Although both PBL schemes accurately simulated the barrier jet, the evolution of the subgrid variables (TKE, l_m, and S_ϕ) were very different. This was somewhat surprising, since only the mixing length specification and tuning of coefficients differed (see Appendix A). The following points highlight the major behavioral differences between the two schemes:

(1) The MYNN generally had larger TKE and mixing length, which led to a slightly larger mixed-layer depth in the MYNN than in the MYJ simulation. The MYNN TKE verified well, but produced TKE even when $Ri > 1$ (not shown). This was likely due to a feedback between the larger mixing lengths and TKE, which produces enhanced vertical redistribution of TKE into regions of higher Ri. In contrast, the MYJ TKE was typically underpredicted, with maximum values typically only about half as large as observed. Also, the MYJ mixing lengths were very small immediately above the gap outflow.

(2) The MYJ generally produced a stronger low-level wind shear, due to a larger surface drag coefficient, C_D (not shown). Comparisons of surface layer fluxes show that the viscous sublayer in the MYJ surface layer scheme produced a discontinuity in the surface fluxes across 16 m s^{-1}. This did not produce a noticeable effect in the mean fields.

(3) The eddy diffusivities, K_ϕ, were much larger in the MYNN then in the MYJ PBL scheme. However, due to the larger low-level vertical gradients in the MYJ, the tendencies produced by each PBL scheme were of similar magnitude. Since the observed surface winds were not measured, it is impossible to tell which scheme produced the more accurate low-level gradients.

(4) The advection of TKE in the MYNN produced a smoother field with slightly decreased magnitudes and eliminated the columnar towers of TKE, which appear unrealistic. However, the impact of TKE advection on the mean fields was negligible.

We believe the SARJET dataset is unique and may be especially valuable as a validation dataset for NWP models, specifically TKE studies in barrier jets. Diagnosis of the WRF model errors over the complex orography of Alaska is a necessary step needed in order to further model development. These results provide a useful benchmark for further testing of next-generation PBL schemes that will be performed in the near future.

Acknowledgments.

The authors thank Carl Dieking of NOAA NWS-Juneau, AK for access to ground-based profiler data (not shown this abstract). This research was supported by a National Research Council (NRC) Fellowship. Use of the WRF-ARW was made possible by the Microscale and Mesoscale Meteorological (MMM) Division of the National Center for Atmospheric Research (NCAR), which is supported by the National Science Foundation.

APPENDIX A

Boundary layer parameterizations

Both schemes start with the same basic form of the turbulent kinetic energy equation:

$$\frac{d(q^2/2)}{dt} - \frac{\partial}{\partial z}\left[l_m q S_q \frac{\partial}{\partial z}\left(\frac{q^2}{2}\right)\right] = P_s + P_b + \varepsilon, \quad \text{(A1)}$$

where the first term on the left-hand side represents the total derivative of $q(= 2 \times TKE)$ and the second term represents the vertical redistribution of q. The terms on the right-hand side of (1A) represent the production of q by shear, buoyancy, respectively, and the last term is the dissipation term. Their forms are as follows:

$$P_s = -(\overline{u'w'})\frac{\partial u}{\partial z} - (\overline{v'w'})\frac{\partial v}{\partial z}, \quad \text{(A2a)}$$

$$P_b = \beta_1 g(\overline{u'\theta_v'}), \quad \text{(A2b)}$$

$$\varepsilon = \frac{q^3}{B_1 l_m} \quad \text{(A2c)}$$

The primary difference between the two schemes is the formulation of the master mixing lengths, l_m, which influences the vertical redistribution term (second term on RHS of A1) and the dissipation term (A2c).

Mellor-Yamada-Janjić master mixing length

Within the PBL, the master mixing length is:

$$l_m = l_0 \frac{kz}{kz + l_0}, \quad \text{(A3)}$$

where l_0 is:

$$l_0 = 0.23 \frac{\int_0^{z_i} zq \quad dz}{\int_0^{z_i} q \quad dz}. \quad \text{(A4)}$$

For small z (in the surface layer), $l_m \rightarrow kz$, where k is the von Karman constant (0.4). For large z (between the top of the surface layer and z_i is the PBL height), $l_m \rightarrow l_0$. Above the PBL,

$$l_m = 0.23 \triangle Z, \tag{A5}$$

where $\triangle Z$ is the models vertical grid spacing. The PBL height is determined to be where q falls below a critical value (0.001 m^2 s^{-2}).

Mellor-Yamada-Nakanishi-Niino master mixing length

The mixing length, l_m, is designed such that the shortest length scale among the, surface layer length, l_s, turbulent length, l_t, and buoyancy length, l_b will dominate:

$$\frac{1}{l_m} = \frac{1}{l_s} + \frac{1}{l_t} + \frac{1}{l_b}. \tag{A6}$$

The surface layer length scale l_s is a function of the dimensionless height ($\zeta = z/L$), where L in the Monin-Obukhov length [$= -u_*^3\overline{\Theta_v}/kg(\overline{w'\Theta'})$]:

$$l_s = \begin{cases} kz/3.7 & \text{if } \zeta > 1, \\ kz(1+2.7\zeta)^{-1} & \text{if } 0 \geq \zeta > 1, \\ kz(1-100\zeta)^{0.2} & \text{if } \zeta < 0. \end{cases} \tag{A7}$$

The turbulent length scale l_t is the same as l_0 (A4 for MYJ), but integrated to $z = \infty$. For stable conditions, the buoyancy length scale l_b is:

$$l_b = \left[1 + 5\left(\frac{q_c}{l_t N}\right)^{1/2}\right]\frac{q}{N}, \tag{A8}$$

where $N = [(g/\theta_0)\partial\theta_v/\partial z]^{1/2}$ and $q_c = [(g/\theta_0)\langle w\theta_v\rangle_s l_t]^{1/3}$. If $N < 0$, then $l_b = \infty$.

The MYNN also uses a partial-condensation scheme, which follows Deardorff (1977) and Mellor (1977). This takes into account condensational processes by assuming a probability distribution of physical quantities around their ensemble averages to be a Gaussian distribution (see Nakanishi and Niino (2004)). Note that there is no dependence on PBL height in the MYNN.

REFERENCES

Blumen, W., R. Banta, S. P. Burns, D. C. Fritts, R. Newsom, G. S. Poulos, and J. Sun, 2001: Turbulence statistics of a Kelvin-Helmholtz billow event observed in the nighttime boundary layer during the Cooperative Atmosphere- Surface Exchange Study field program. *Dyn. Atmos. Oceans*, **34**, 189–204.

Bond, N. A., C. F. Dierking, and J. D. Doyle, 2006: Research aircraft and wind profiler observations in Gastineau Channel during a Taku wind event. *Wea. Forecasting*, **21**, 489–501.

Colle, B. A., K. A. Loescher, G. S. Young, and N. S. Winstead, 2006: Climatology of barrier jets along the Alaskan Coast. Part II: Large-scale and sounding composites. *Mon. Wea. Rev.*, **134**, 454–477.

Colman, B. R. and C. F. Dierking, 1992: The Taku wind of southeast Alaska: Its identification and prediction. *Wea. Forecasting*, **7**, 49–64.

Deardorff, J. W., 1977: A parameterization of ground-surface moisture content for use in atmospheric prediction models. *J. Appl. Meteor.*, **16**, 1182–1185.

Dierking, C. F., 1998: Effects of a mountain wave windstorm at the surface. *Wea. Forecasting*, **13**, 606–616.

Esau, I. N. and Ø. Byrkjedal, 2007: Application of a large eddy simulation database to optimization of first-order closures for neutral and stably stratified boundary layers. *Bound.-Layer Meteor.*, **125**, 207–225.

Grell, G. A. and D. Devenyi, 2002: A generalized approach to parameterizing convection combining ensemble and assimilation techniques. *Geophys. Res. Lett.*, **29(14)**, Article 1693.

Howell, J. and J. Sun, 1997: Surface layer fluxes in stable conditions. *Bound.-Layer Meteor.*, **90**, 495520.

Janjić, Z. I., 2002: Nonsingular implementation of the Mellor-Yamada level 2.5 scheme in the NCEP Meso model. NCEP Office Note No. 437, 61 pp pp.

Loescher, K. A., G. S. Young, B. A. Colle, and N. S. Winstead, 2006: Climatology of barrier jets along the Alaskan Coast. Part I: Spatial and temporal distributions. *Mon. Wea. Rev.*, **134**, 437–453.

Mahrt, L., 1998: Stratifed atmospheric boundary layers and breakdown of models. *J. Theor. Comput. Fluid Dyn.*, **11**, 263–280.

Mahrt, L., 1999: Stratified atmospheric boundary layer. *Bound.-Layer Meteor.*, **90**, 375–396.

Mellor, G. L., 1977: The gaussian cloud model relations. *J. Atmos. Sci.*, **34**, 356–358 and 1483–1484.

Mlawer, E. J., S. J. Taubman, P. D. Brown, M. J. Iacono, and S. A. Clough, 1997: Radiative transfer for inhomogeneous atmosphere: RRTM, a validated correlated-k model for the longwave. *J. Geophys. Res.*, **102, (D14)**, 16 663–16 682.

Nakanishi, M. and H. Niino, 2004: An improved Mellor-Yamada level-3 model with condensation physics: Its design and verification. *Bound.-Layer Meteor.*, **112**, 1–31.

Nappo, C., 1991: Sporadic breakdowns of stability in the PBL over simple and complex terrain. *Bound.-Layer Meteor.*, **54**, 69–87.

Olson, J. B., B. A. Colle, N. A. Bond, and N. Winstead, 2008: A comparison of two coastal barrier jet events along the southeast Alaskan Coast during the SARJET field experiment. *Mon. Wea. Rev.*, **135**, 3642–3663.

Skamarock, W. C., J. B. Klemp, J. Dudhia, D. O. Gill, D. M. Barker, W. Wang, and J. G. Powers, 2008: A description of the advanced research WRF version 3. NCAR Tech. Note NCAR/TN 475+STR, 113 pp. pp.

Smirnova, T., J. M. Brown, S. G. Benjamin, and D. Kim, 2000: Parameterization of cold season preocesses in the MAPS land-surface scheme. *J. Geophys. Res.*, **105(D3)**, 4077–4086.

Thompson, G., R. M. Rasmussen, and K. Manning, 2004: Explicit forecasts of winter precipitation using an improved bulk microphysical scheme. Part I: Description and sensitivity analysis. *Mon. Wea. Rev.*, **132**, 519–542.

Wang, H., W. C. Skamarock, and G. Feingold, 2009: Evaluation of scalar advection schemes in the Advanced Research WRF model using large-eddy simulations of aerosol-cloud interactions. *Mon. Wea. Rev.*, In press.

Winstead, N. S., et al., 2006: Barrier jets: Combining SAR remote sensing, field observations, and models to better understand coastal flows in the Gulf of Alaska. *Bull. Amer. Meteor. Soc.*, **87**, 787–800.

Zhang, D.-L. and W.-Z. Zheng, 2004: Diurnal cycles of surface winds and temperatures as simulated by five boundary layer parameterizations. *J. Appl. Meteor.*, **43**, 157–169.

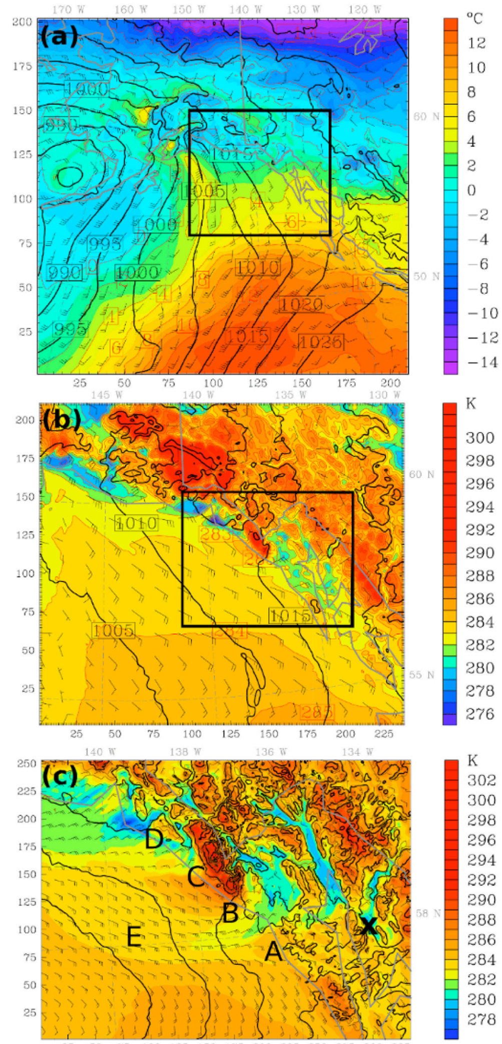

Fig. 1. Sea-level pressure (black contours), temperature (color), and winds (black barbs) for (a) 13-km domain at 1200 UTC, (b) 4.33-km domain at 1800 UTC, and (c) 1.44-km domian at 0000 UTC 12-13 October 2004. The points of the flight track are marked A-E and the South Douglass profiler marked as "x". Note that potential temperature is used for (b) and (c) to highlight the inland cold pool.

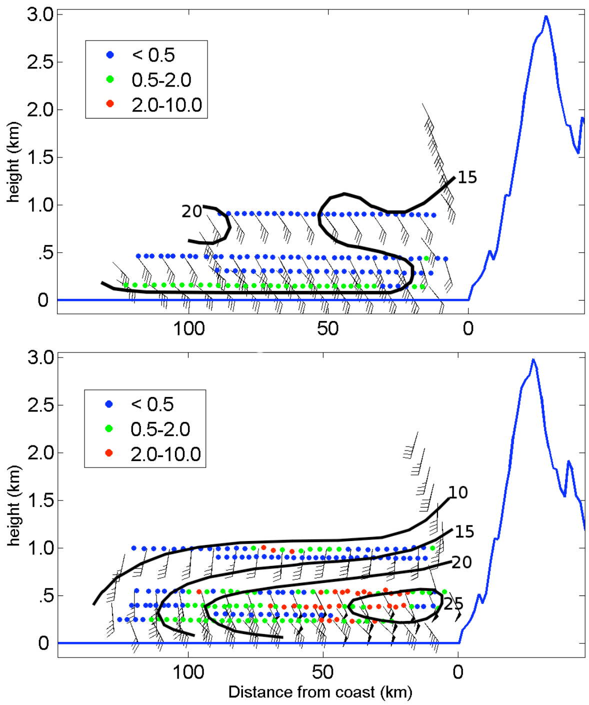

Fig. 2. Observed coast-parallel wind speeds (black contours; every 5 m s^{-1}), TKE (colored dots; m^2 s^{-2}), and wind barbs (full barb = 5 m s^{-1}) for (a) flight 1: 1800-2100 UTC 12 October 2004 and (b) flight 2: 0000-0300 UTC 13 October 2004 across the hybrid barrier jet.

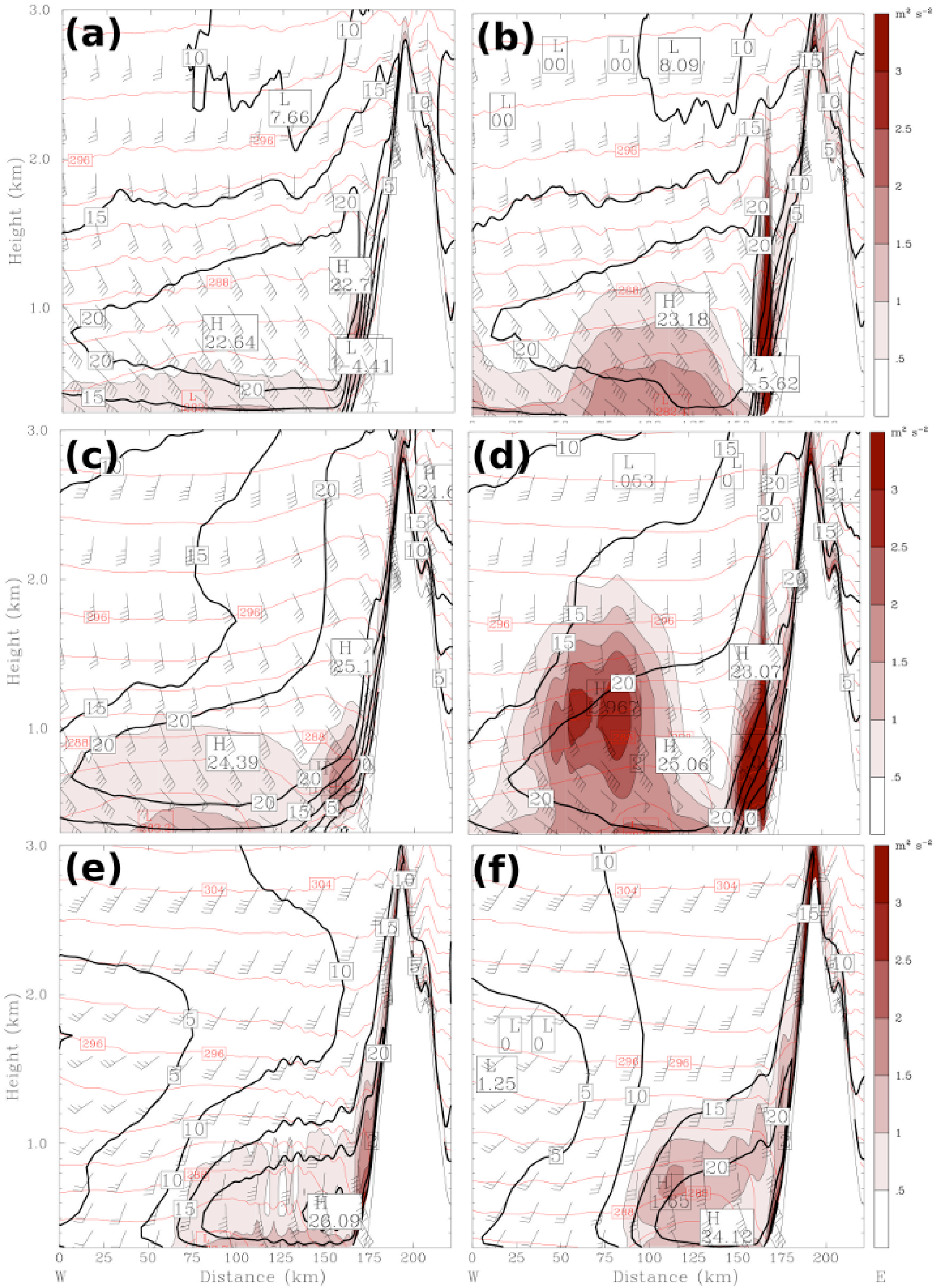

FIG. 3. Evolution of the model TKE between point C-E (see Fig. 1c) for the MYJ (left) and MYNN (right). (a-b) 2300 UTC (c-d) 0100 UTC, and (e-f) 0300 UTC 12-13 October 2004.

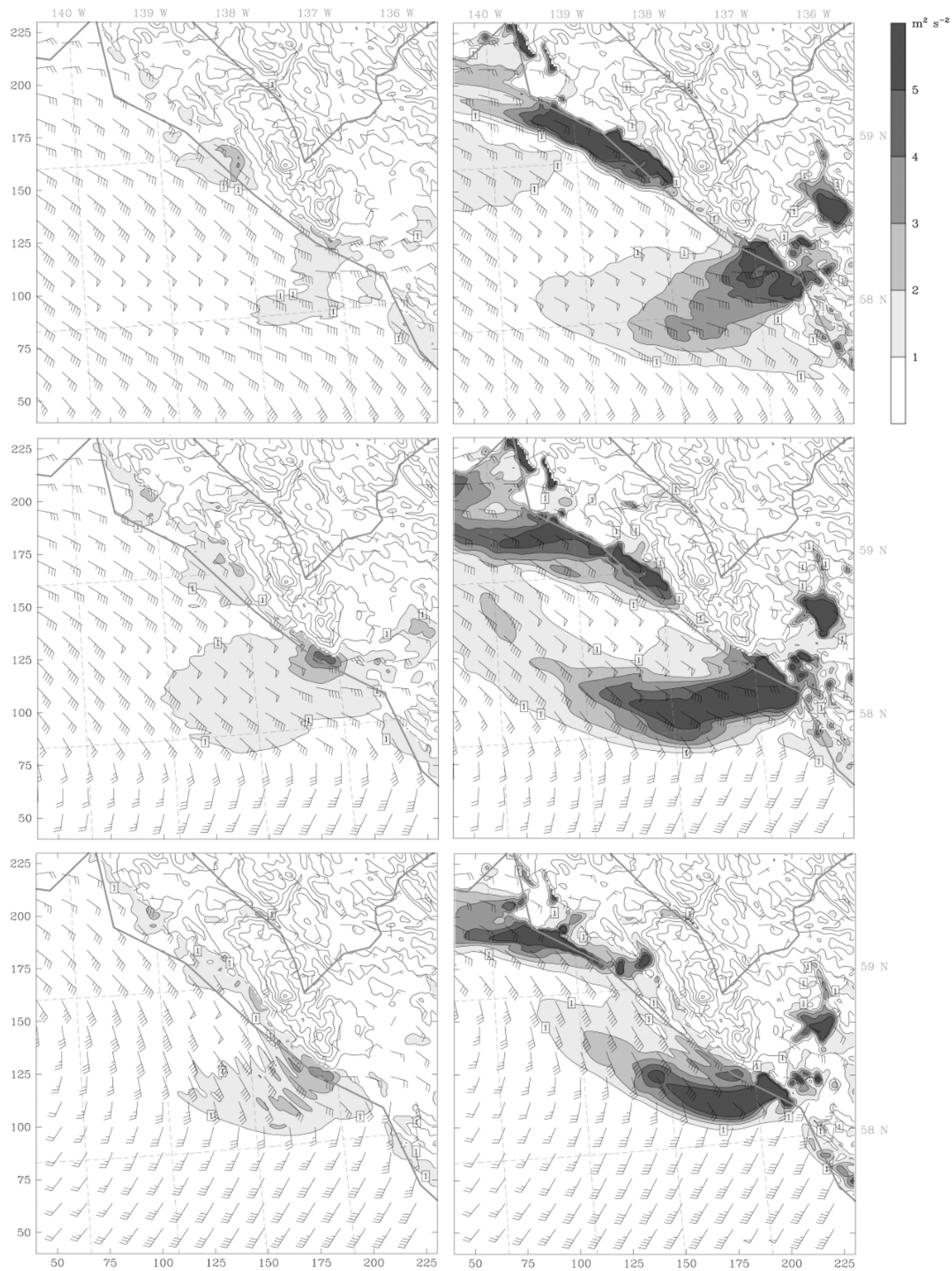

Fig. 4. Evolution of the model TKE at 500 m MSL for the MYJ (left) and MYNN (right). (a-b) 2300 UTC (c-d) 0100 UTC, and (e-f) 0300 UTC 12-13 October 2004.

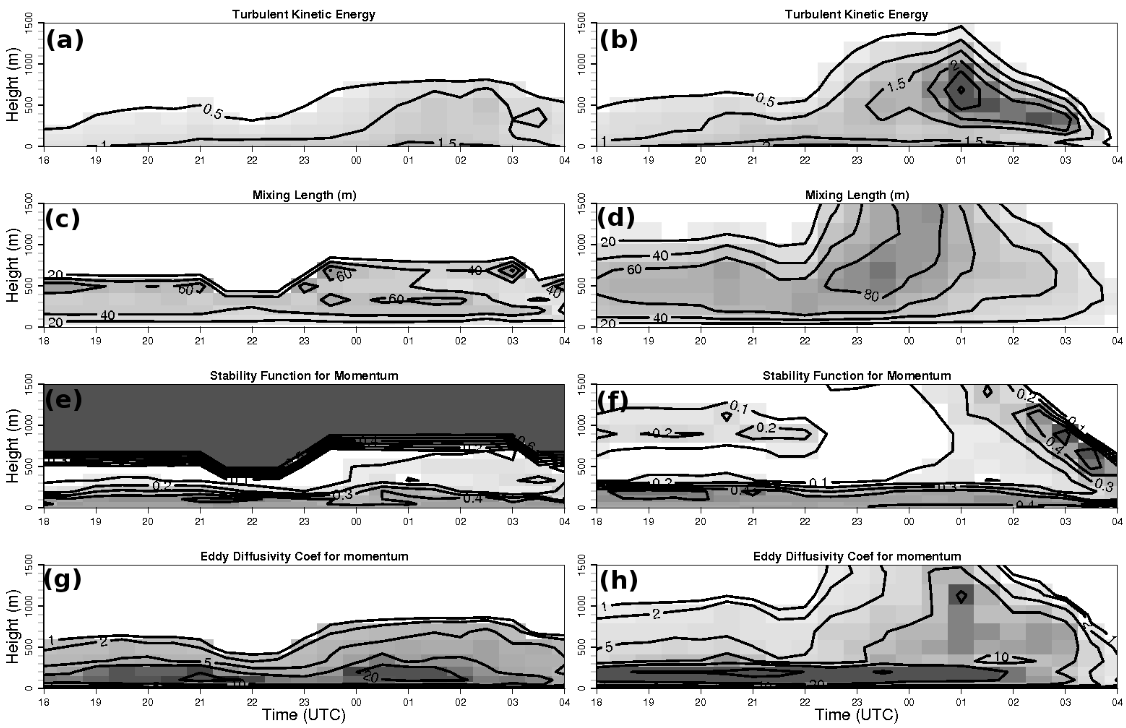

FIG. 5. Evolution of the model (a-b) TKE, (c-d) mixing length, (e-f) stability function for momentum, and (g-h) K_m between the surface and 1500 m ASL through the hybrid barrier jet (SW of the Fairweathers, see Fig. ??c) for the MYJ (left) and MYNN (right) between 18 UTC 12 October and 04 UTC 13 October 2004.

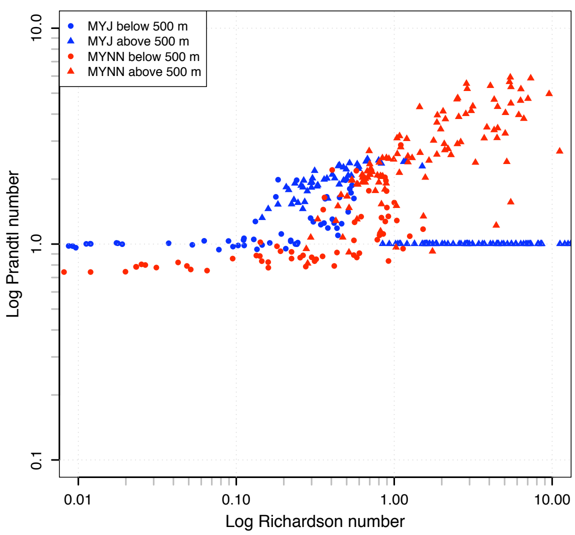

Fig. 6. The model Pr as a function of Richardson number. MYJ (blue) and MYNN (red). Values below 500 m MSL (within hybrid jet) are circles and above 500 m are triangles.

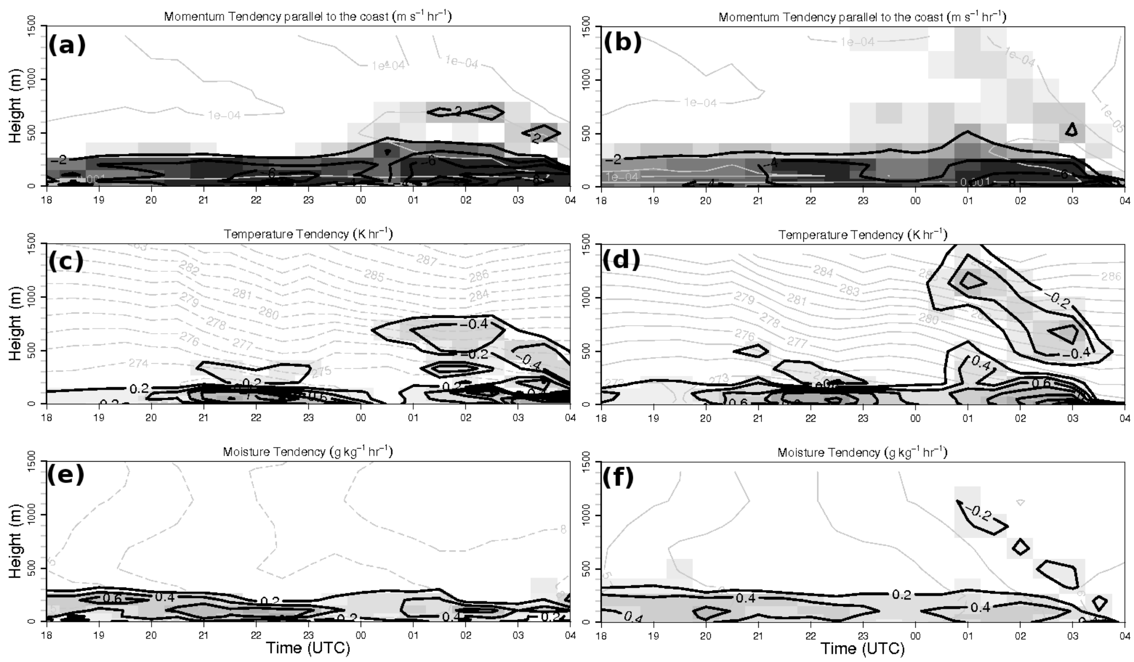

FIG. 7. Evolution of the model PBL tendencies for (a-b) momentum, (c-d) heat, and (e-f) moisture between the surface and 1500 m MSL through the hybrid barrier jet (SW of the Fairweathers, see Fig. **??**) for the MYJ (left) and MYNN (right) between 18 UTC 12 October ans 04 UTC 13 October 2004. The background gray contours are (a-b) vertical wind shear (s^{-1}), (c-d) potential temperature (K), and (e-f) mixing ratio (g kg^{-1}).

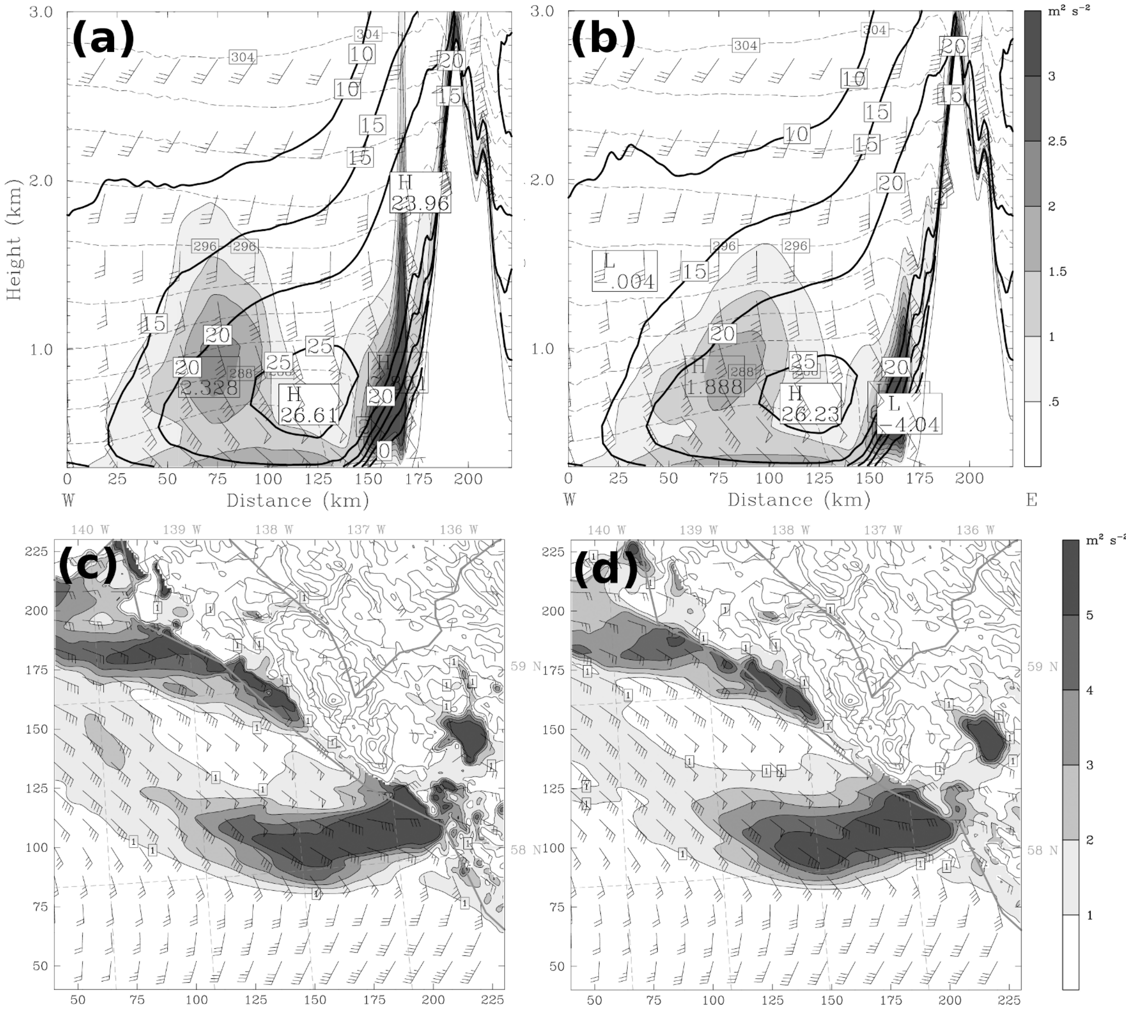

Fig. 8. Comparison of the MYNN simulation with and without TKE advection. The top row shows the coast-parallel wind speeds, potential temperature, and TKE for (a) the control simulation (without TKE advection) and (b) TKEADV simulation. The bottom rows show the winds and TKE at 500 m MSL for (c) the control simulation and (d) TKEADV simulation for 0100 UTC 13 October 2004.